ISIJ International, Vol. 61 (2021), No. 3, pp. 881–887
https://doi.org/10.2355/isijinternational.ISIJINT-2020-591

Early Precipitation Stages of Sigma Phase in Alloy 28 Studied with Scanning Electron Microscopy and Atom Probe Tomography

Claes-Olof A. OLSSON,[1)] Mats HÄTTESTRAND,[2)] Hans MAGNUSSON,[3)] Deodatta SHINDE[4)] and Mattias THUVANDER[5)]*

1) École Polytechnique Fédérale de Lausanne, CH-1015 Lausanne, Switzerland.
2) Sandvik Materials Technology, SE-811 81 Sandviken, Sweden.
3) Swerim AB, PO Box 7047, SE-164 07 Kista, Sweden.
4) Dept. of Physics, Chalmers University of Technology. Now at Materials Science Division, Bhabha Atomic Research Centre, Mumbai-400085, India.
5) Dept. of Physics, Chalmers University of Technology, SE-412 96 Gothenburg, Sweden.

(*Received on September 30, 2020; accepted on November 25, 2020*)

This study deals with early stages of sigma phase growth in a high end austenitic stainless steel – Alloy 28 (EN 1.4563/UNS N08028). Its precipitation kinetics was followed by a series of heat treatments at 800°C for holding times up to 30 000 s. The samples were studied with high resolution scanning electron microscopy and atom probe tomography. Detailed image analysis of the micrographs made it possible to quantify the growth rate of the precipitates. It was shown that diffusion limited growth along grain boundaries was about 15 times faster than growth perpendicular to a grain face. By combining the image data with quantitative chemical analysis of the phase boundaries, it was possible to estimate diffusion coefficients in the lattice and in the grain boundaries; grain boundary diffusion coefficients were about 250 times those of the lattice.

KEY WORDS: sigma phase; stainless steel; scanning electron microscopy; atom probe tomography; lattice diffusion; grain boundary diffusion.

1. Introduction

A critical point when developing high end stainless steels is to avoid embrittlement by sigma phase. Many of the elements that have a strong positive influence on the corrosion resistance, *e.g.* chromium and molybdenum, are also sigma phase stabilizers.[1,2)] The sigma phase has space group number 136, $P4_2/mnm$, and is considerably harder than ferrite and austenite. It has a relatively wide composition range, where Cr contents may vary between 30 and 50 wt%, and Mo can be enriched up to five times its bulk content. It is possible to avoid sigma phase by increasing the stability of the bulk, for example by adding nickel. The alloy in this study, Alloy 28 (EN 1.4563/UNS N08028), is rich in Cr (26 wt%) and Mo (3.3 wt%), and it has a relatively high Ni content (30 wt%). The precipitation kinetics in Alloy 28 is much slower than in austenites with a lower Ni content, *e.g.* EN 1.4547/UNS32154, and at least one order of magnitude slower than in two-phase materials such as EN 1.4410/UNS32750.[3)] This makes Alloy 28 a good candidate for studies of early stages of sigma precipitation. Another advantage is that it precipitates almost only sigma at 800° C.

The formation of sigma phase in stainless steel, and the influence of composition and aging, as well as the effects on mechanical and corrosion properties, has been extensively studied over the years.[4–9)] A recent review of sigma phase has been written by Hsieh and Wu.[3)] Studies in detail on the precipitation kinetics for longer times have been made, for example by Erneman *et al.*, who quantified the influence of silicon for incorporation in thermodynamic databases.[10)] Perron *et al.* made a comparative study between Thermo-Calc and MatCalc and found calculated time-temperature-precipitation diagrams to be in good agreement with experimental data for duplex stainless steels.[11)] As in this study, they found most sigma precipitates at grain boundaries, at least in solution treated material. The thermodynamics of sigma phase stability has recently been revisited by Jacob *et al.*, who suggested a revised thermodynamic description of the Fe–Cr system based on an improved sublattice model.[12)] The same group later continued to expand this concept to duplex stainless steels.[13)] In a recent paper, Laplanche *et al.* studied sigma precipitation in a high entropy CrMnFeCoNi alloy.[14)] They used exposure times from 3 minutes to 1 000 hours, and fitted growth curves to the Johnson-Mehl-

* Corresponding author: E-mail: mattias.thuvander@chalmers.se

Avrami-Kolmogorov model.[14] The dynamics of the system were approximated by an Arrhenius expression. Apart from the obvious difference in composition to the material used here, their material was small amounts of vacuum induction melted material, swaged to a rod, as opposed to commercially produced wire. Among other things, this affects the amount of grain boundaries available for nucleation as well as the relative orientations of grains, both important properties that influence precipitate kinetics. Sigma phase growth in austenitics has been studied in detail by Schwind *et al.*, who designed a model for precipitation in austenitic stainless steels and found the shape of grains to be of minor importance compared to their size.[15] They studied heat treatments up to several thousand hours. In the present study, the time frame is shorter, ranging from minutes to hours. Another study of the long-term evolution of sigma phase was made by Ji *et al.*, who combined experimental and computational methods to look at precipitation after times as long as 18 years.[16] Warren *et al.* studied shorter times, and investigated a duplex stainless steel, EN 1.4462/UNS S31803 (22Cr5Ni3Mo), for exposures up to 100 hours. In addition to more conventional methods, they also used magnetic force microscopy to quantify the presence of sigma as well as austenite and ferrite in the matrix. For duplex stainless steels, the kinetics are somewhat different compared to single phase austenitics. The sigma phase can nucleate on an austenite grain face, where there is a good lattice match, and then grow into the ferrite, where sigma phase stabilizers such as chromium and molybdenum are present to a higher extent.[17] For many duplex stainless steels, the precipitation velocity of sigma phase is higher than for austenitic grades with the corresponding amount of sigma stabilizers.

In this study, we focus on the initial stages of sigma phase precipitation. Selected locations of the material heat treated for 10 ks were used for further study with Atom Probe Tomography (APT) to obtain sub-nm resolution in the characterization of the sigma/austenite interface. APT has already been used to characterize different types of interfaces for correlation with thermodynamical parameters; a review of such studies has been written by Andrén.[18]

2. Experimental

2.1. Material

The material used for this study was Alloy 28 (EN 1.4563/UNS N08028) with the heat composition given in **Table 1** in wt%, together with the normalized concentration in at.% for reference. Its shape was Ø2.3 mm wire. A dilatometer was used to perform the heat treatments. The samples were first solution annealed at 1 150°C for five minutes, then kept at target temperature 800°C for the assigned time (with a cooling rate of about 300°C/s from 1 150°C to 800°C), and finally rapidly quenched to room temperature. The times at target temperature were 100, 300, 1 000, 3 000, 10 000, and 30 000 s. Prior to analysis in the scanning electron microscope, the samples were wet ground to 4 000 mesh. Avoiding polishing, with micron sized particles in suspension, proved to give the best contrast for the sigma particles. This preparation left more cold deformation in the surrounding austenite, creating a good contrast to the sigma particles. The draw-back was some scratches in the images.

Table 1. Heat composition (wt%) together with calculated atomic concentrations for the material in this study.

Element	C	Si	Mn	Cr	Ni	Mo	Cu	Fe
wt%	0.017	0.49	1.7	26.5	30.3	3.3	1.0	36.7
at.%	0.08	1.0	1.7	28.6	29.0	1.9	0.9	36.9

2.2. Scanning Electron Microscopy

The scanning electron micrographs were recorded using a Zeiss Sigma VP equipped with a field emission gun. Images were obtained using the backscatter detector at a nominal magnification of 1 000. The image acquisition pattern in the cross section is given in **Fig. 1**. A total of 25 fields were acquired at the center of each cross section, covering an area of approximately 1×1 mm^2. To improve quantification, the images were acquired and stored as $3\,072\times2\,304$ pixels. This resulted in a pixel size of 37 nm, corresponding to an acquired image size of 110×85 μm. The acceleration voltage was 5 kV giving an estimated information depth and lateral resolution for the backscattered electrons of about 40 nm.

2.3. Image Analysis on Backscattered Electron Micrographs

The image processing algorithms were developed using MATLAB release 2019a together with the corresponding toolbox. Binarization was performed by manual thresholding. The resulting binary image was then cleaned, removing smaller particles based on shape and size. Scratches were identified in the image by means of a Hough transform. A scratch was defined as a straight line with a length of at least half the image height. The pixels forming a line according to this definition were removed from subsequent processing. Parameters extracted included overall phase fraction, number of precipitates and a set of size parameters such as length, width, particle area, *etc.* Definitions for most param-

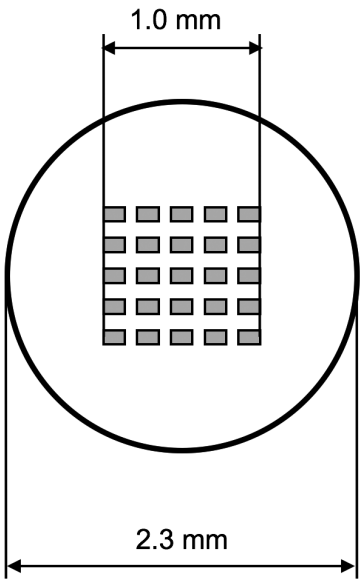

Fig. 1. Schematic showing the positioning of micrographs at the center of the wire cross-section.

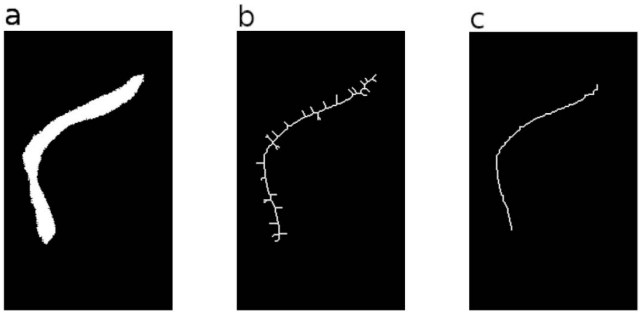

Fig. 2. Schema for calculating the average precipitate thickness. The area of the particle in (a) is calculated, before skeletonization to (b) and pruning to the shape in (c). The length is then integrated along the true pixels in (c).

eters, as well as methods for their extraction, can be found in general textbooks, such as Gonzalez-Woods.[19] The average precipitate thickness was estimated by taking the ratio between the total particle area, *i.e.* all pixels in a connected component, divided by component length. The process of finding particle length is illustrated in **Fig. 2**. Before further processing, the total area of the particle was calculated (Fig. 2(a)). To avoid excessive pruning, the surface was smoothed by eroding the particle with a disk-shaped structural element with a size 5% of the total particle area. The precipitate skeleton is shown in Fig. 2(b) and after pruning in Fig. 2(c). The particle length was calculated by summing up the distances between each pixel: if the nearest neighbor is horizontally or vertically aligned, the distance is 1 pixel, if it is diagonally aligned, the distance is $\sqrt{2}$ pixel. This procedure was verified by a set of test figures with known distances testing all possible orientations.

2.4. Atom Probe Tomography

Samples for APT where prepared using a standard FIB/SEM lift-out procedure,[20] whereby sigma particles located at grain boundaries were targeted. The instrument used was an FEI Versa 3D. The atom probe instrument used was a LEAP 3000X HR (Imago Scientific Instruments), which has a laser wavelength of 532 nm, and the experiments were done using laser pulsing with pulse energy of 0.15 nJ at 200 kHz, and a sample set temperature of 50 K in combination with an acquisition rate of 0.5%. The data was evaluated using the software IVAS 3.6.14 (Cameca). The reconstructions were made using the voltage method with a field of 25 V/nm, field factor of 4.0 and an image compression factor of 1.65. Concentration profiles across the sigma/austenite interface were constructed as proximity histograms (proxigrams) from iso-concentration surfaces. The voxel size was 1.0 nm^3 and the delocalization distance was $3.0\times3.0\times1.5$ nm^3.

3. Results

3.1. Quantitative Image Analysis of the Scanning Electron Micrographs

Images for analysis were acquired in high resolution, **Fig. 3**(a), and processed as indicated above into a binary image as exemplified in Fig. 3(b). Phase fractions were calculated as the sum of all true (white) pixels over the total image size, and then summed up for the set of 25 images belonging to each analyzed cross section. The phase fraction as a function of time is illustrated in **Fig. 4**. No particles were seen in any of the 25 fields acquired from the sample aged for 100 s, and only a few were found in the 300 s sample. Thus, there appears to be an initial nucleation period of about 300 s, before the onset of logarithmic growth. It is also interesting to follow the development of the number of particles as a function of time. For this purpose, a set of histograms for each aging time is presented in **Fig. 5**. All particles were located at grain boundaries. There also appears to be a strong orientation dependence on nucleation, as even at

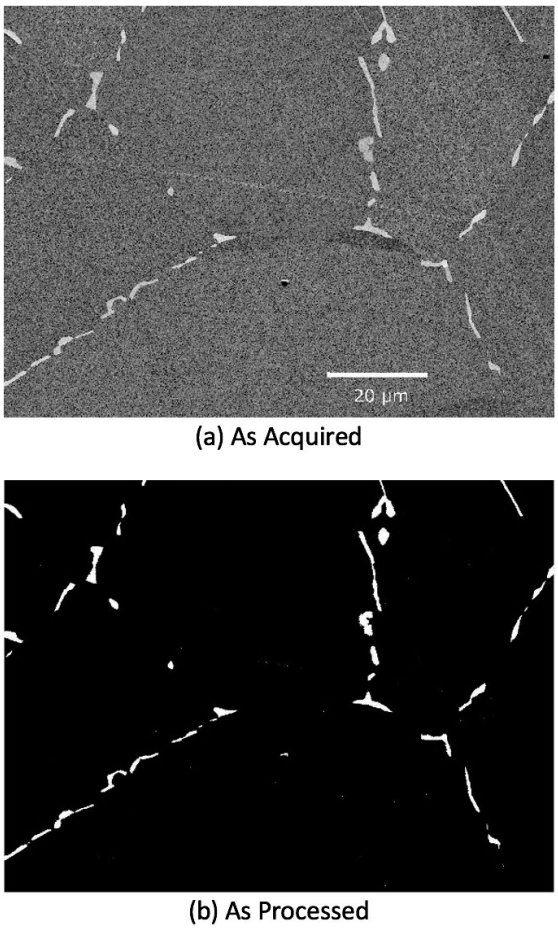

Fig. 3. Scanning electron micrographs recorded for a sample aged 30 ks, before (a) and after (b) image processing. The sigma phase precipitates are found along the grain boundaries.

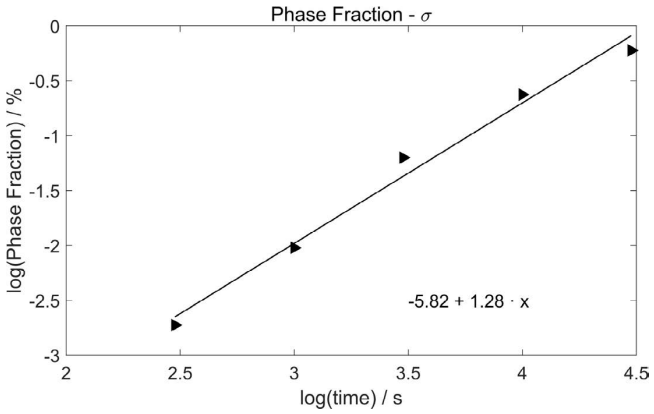

Fig. 4. Logarithm of the phase fraction of sigma as a function of log (time). After an initial incubation time of about 300 s, the precipitates followed a log-log rate law.

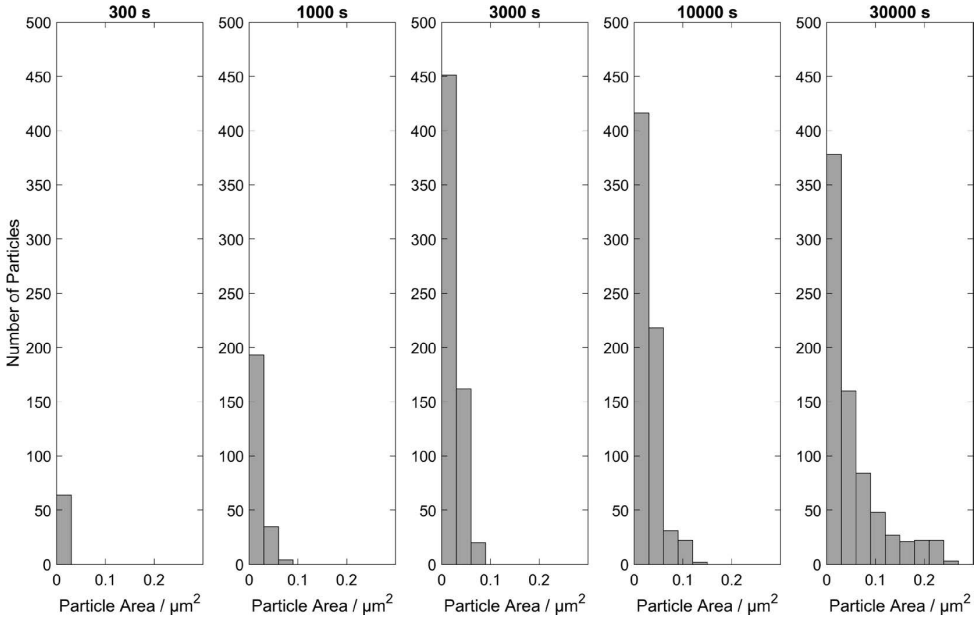

Fig. 5. Particle size histograms for the different times studies. The maximum value in the smallest particle bin is reached after 3 ks.

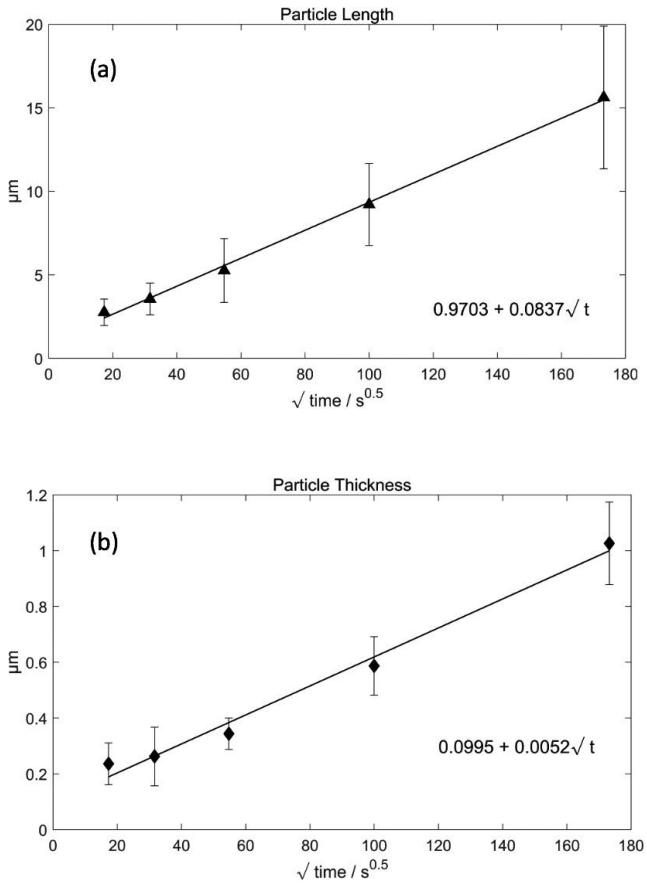

Fig. 6. Sigma precipitate size parameters taken from the top 10th area percentile.

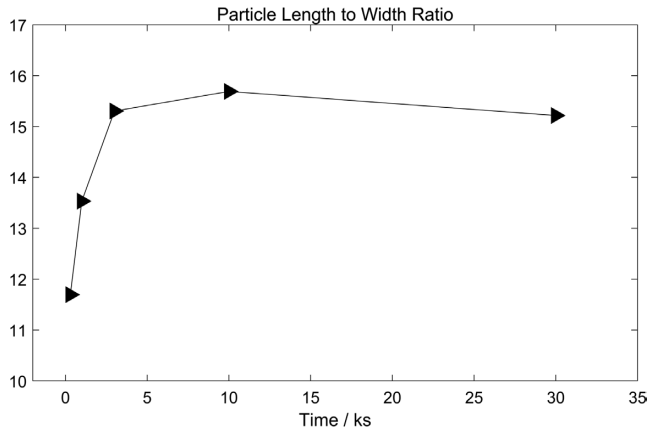

Fig. 7. Length to width ratio of the top 10th area percentile.

30 ks, there were precipitate free fields of view, despite the presence of grain boundaries. The smallest size class, starting at a feret diameter of 40 nm, has a maximum at 3 ks. This gives the perception of an initial time span where a mechanism other than diffusion limited growth could be considered rate limiting. In the longer term, when all grain boundaries are filled with sigma phase, there will normally also be secondary phase particles within the grains. This study focused on initial stages of precipitation, so the stage where particles form inside the grains was not reached. As all particles were located at grain boundaries, it was of interest to measure their length and width dependence on aging time. The respective graphs are shown in **Fig. 6**. For both these plots, the particles belonging to the top 10th percentile were used. Hence, the particles studied are those with the most favorable growth conditions in combination with a sectioning close to the largest particle dimensions. The length, as well as the width, follows a square-root dependence with respect to time, indicating that the precipitate growth is diffusion limited in both directions. After an initial nucleation, the dimensionless parameter length/width stabilizes just above 15, as can be seen in **Fig. 7**.

3.2. Atom Probe Tomography at an Austenite/Sigma Interface

Three analyses were made at grain boundaries after heat treatment at 800°C for 10 ks, all with similar results. All positions were taken across a phase boundary between austenite and sigma phases. In all cases, the interface is atomi-

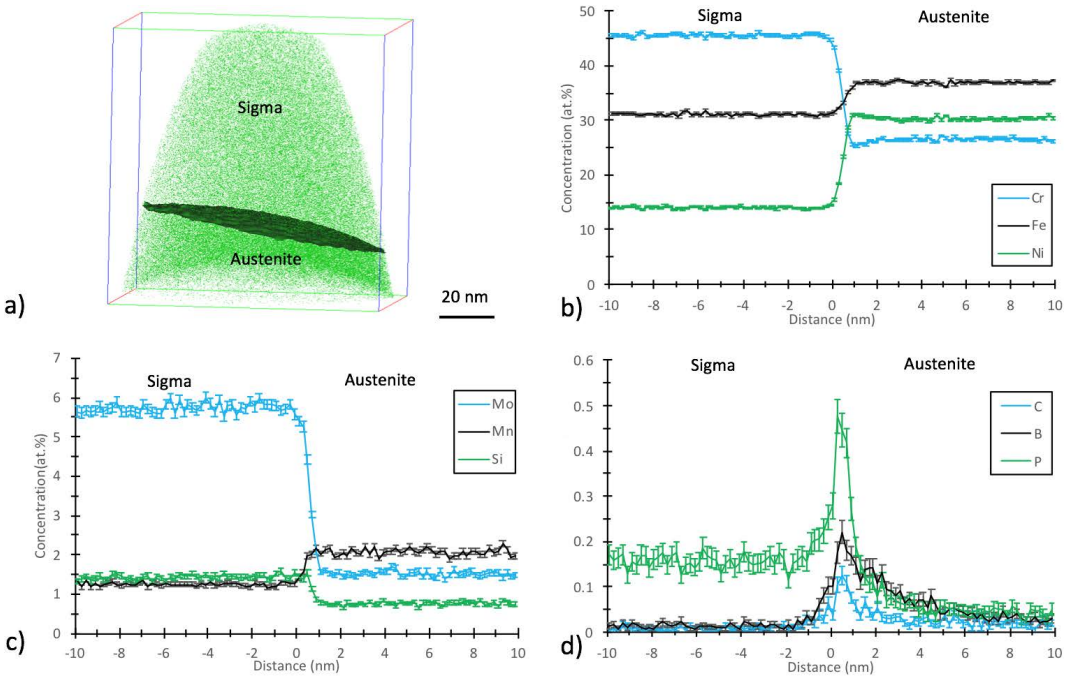

Fig. 8. (a) APT reconstruction showing the distribution of nickel atoms and an iso-surface highlighting the sigma/austenite interface. Proxigrams were established for major elements (b), minor elements (c) as well as trace elements enriched at the interface (d). (Online version in color.)

Table 2. Composition of austenite and sigma phase in at.%. The compositions were averaged at a distance from the austenite/sigma phase, defined by a reconstruction with an iso-concentration surface of Ni at 19 at%.

Element	Sigma phase	Austenite
B	0.005 ± 0.001	0.007 ± 0.003
C	0.001 ± 0.001	0.011 ± 0.002
Si	1.45 ± 0.01	0.77 ± 0.01
P	0.17 ± 0.01	0.028 ± 0.002
Cr	46.4 ± 0.04	27.3 ± 0.06
Mn	1.17 ± 0.01	2.03 ± 0.02
Fe	30.9 ± 0.04	37.5 ± 0.07
Ni	13.5 ± 0.03	29.8 ± 0.07
Mo	6.09 ± 0.02	1.26 ± 0.02

cally sharp, extending for less than 1 nm, reaching the final constant concentrations within that distance; no diffusion gradients were observed. **Figure 8** shows the iso-concentration surface placed at 19 at% Ni (Fig. 8(a)), which is used as the defining boundary for calculating the proxigrams in Figs. 8(b)–8(d). As expected, Cr, Mo and Si are enriched in the sigma phase, whereas Fe, Ni and Mn are depleted. There is also some enrichment of the minor elements P, C and B at the interface. The composition of the sigma phase and the austenite, averaged at a distance from the interface is shown in **Table 2**. In this evaluation, peak overlaps have been corrected for using the natural abundance of isotopes and the background was subtracted using the built-in function of the IVAS software.

4. Discussion

The objective of the present study is to investigate early stages of sigma phase precipitation in an austenitic stainless steel. To reach holding and quench times that are short relative to the precipitation kinetics, it was chosen to work with a steel grade with comparatively slow kinetics: Alloy 28. In an attempt to reach low detection limits, 25 micrographs in high resolution were collected on each cross section for all holding times. With the procedure described above, it was possible to quantify precipitates on a ppm level, see Fig. 4. As all precipitates were located at grain boundaries, it was not possible to explain the data using models for homogeneous nucleation. The first precipitates were found after 300 s; the present parameters allowed for detecting particles with a feret diameter larger than 40 nm. The maximum number of small particles was seen after 3 000 s, see Fig. 5. This period of initial growth could be interpreted as a nucleation stage, before diffusion limited growth in two directions becomes dominant. By studying the length and width development of the precipitates, a linear relation is obtained after the first 1 000 s in the d *vs.* $\sqrt{t}$ plot, see Fig. 6. Another interesting parameter, the ratio between length and width of the largest particles, reaches a plateau of 15 at 3 ks and then remains stable for the durations studied. There is an upper limit to this factor as the precipitates grow longer and start to coalesce in the length direction. The atom probe data of the sigma/austenite interfaces showed very sharp transitions – the lateral extensions were consistently less than 1 nm. This sharpness could be taken as motivation for using a simple model for diffusion limited growth. If all sigma stabilizers that reach the interface create precipitate material, *i.e.* their concentration on the austenitic side will effectively be at the matrix bulk content, even though the interface is moving. This approximation makes it possible to use the Cottrell

solution[21] to Fick's equations for material transport:

$$\frac{\partial n_i}{\partial t} = \frac{A\sqrt{D_i^\gamma}}{\sqrt{\pi t}} \frac{c_i^\gamma \rho^\gamma}{M^\gamma} \quad \text{..... (1).}$$

In Eqs. (1), and (2)–(4) below, the following quantities are used

- n_i - number of element i (mol/cm^3)
- t - time (s)
- A - area of the interface (cm^2)
- d - particle size perpendicular to A (cm)
- M^γ - molar mass of the austenite (g/mol)
- c_i^γ - concentration of element i in the austenite
- c_i^σ - concentration of element i in the sigma phase
- ρ^γ - density of the austenite (g/cm^3)
- D_i^γ - diffusion constant of element i in the austenite (cm^2/s)
- k - slope in the graphs, see Figs. 6(a)–6(b), (cm/s$^{1/2}$).

The extension of the sigma phase, as determined by image analysis, will be the integral of this solution. As the lengths and widths of the largest particles have been determined, cf. Figure 6, the quantity $\partial d/\partial t$ is obtained from the linear fit constant as

$$\frac{\partial d}{\partial t} = \frac{k}{2\sqrt{t}} \quad \text{..... (2).}$$

Equation (1) expresses the material transport across the austenite/sigma interface, which can be directly related by stoichiometry to the sigma phase growth rate. Assume all growth is perpendicular to a grain face, limited by element i, which has an austenite content of c_i^γ and a different atomic concentration in the sigma phase c_i^σ. It is only necessary for the additional Cr or Mo needed to diffuse into the particle region to stabilize the sigma phase arrangement. Hence, for growth at two opposite interfaces:

$$\frac{\partial n_i}{\partial t} = A\frac{\rho^\sigma}{M^\sigma}\left(c_i^\sigma - c_i^\gamma\right)\frac{k}{4\sqrt{t}} \quad \text{..... (3).}$$

By equating Eqs. (3) and (1), it is possible to express the diffusion coefficient in the austenite D_i^γ for element i as

$$D_i^\gamma = \frac{\pi (k/2)^2}{4}\left(1 - \frac{c_i^\sigma}{c_i^\gamma}\right)^2 \quad \text{..... (4).}$$

The expression is simplified by assuming that the density to molar mass ratio ρ/M is similar in the precipitate and in the bulk. It is also assumed that sigma formation is rate limited by one, or perhaps two, sigma stabilizers in the bulk. It is possible that both Mo and Cr simultaneously limit growth, as they both take the same positions in the precipitate crystal structure. The opposite condition, that sigma phase formation could be limited by depletion of austenite stabilizers is also possible, but was considered less likely, given the shape of the sharp gradients at the phase boundaries, as illustrated in Fig. 8. Diffusion coefficients calculated from Eq. (4) can be found in **Table 3**, whereby the concentrations come from Table 2, and the values of k are taken from Figs. 6(a)–6(b), *i.e.* 0.0837 μm/s$^{-1/2}$ and 0.0052 μm/s$^{-1/2}$, for grain boundary and lattice, respectively. Values are given for two sigma stabilizers (Cr and Mo), and two elements with higher affinity to the matrix (Fe and Ni). Values from the DICTRA database calculated using TCFE9 are also given for comparison.[22] These values are the result of a weighted assessment of a large set of literature data,[23] mostly obtained using diffusion of ^{51}Cr. The best matches are found for Cr and Fe lattice diffusion. It thus appears possible that both Fe egress from, as well as Cr ingress into, the sigma phase could be rate limiting, or that there is a balance between the two diffusion processes. A set of experiments using alloys with different compositions could possibly elucidate this method further. As the Ni content of the matrix is quite high, it is also worth noting that the values presented here also compare well with those established for Ni-base alloys, for example by Paul *et al.*[24] For grain boundary diffusion, the literature shows quite a large spread.[25–28] One advantage with the method used in this paper is that the length is estimated directly on a particle with diffusion limited growth, and that it also gives correct values for particles following grain boundaries with an arbitrary shape. The method most frequently found in the literature is attenuation of the ^{51}Cr signal with depth, following a series of heat treatments. With indirect methods, it is not possible to separate lattice, grain boundary and deformation enhanced diffusion, but a series of assumptions have to be made concerning for example grain boundary width.[29] Another method to study diffusion is by analyzing interface broadening on cross sections, as illustrated in a recent study by Prasanthi *et al.*[30] Their interdiffusion values in 304L compare by order of magnitude with the values in Table 3. Still, this method also has the drawback of not directly accounting for the influence of curved grain boundaries and cold deformation. As most literature values for lattice diffusion are measured on materials containing both cold deformation and grain boundaries, whereas the material in the present study has no or little cold deformation, and also estimates lattice diffusion in regions perpendicular to a grain boundary, it appears reasonable that the values in Table 3 are slightly below most literature data. From Fig. 7, it is concluded that the length to width ratio of precipitates is constant at 15 for times shorter than 30 ks. This corresponds to a ratio between grain boundary and lattice diffusion coefficients of 254, calculated as the square of the slopes in Fig. 6. The best agreement with literature data was found for Cr and Fe diffusion coefficients. For sigma formation, there is an enrichment of Cr and depletion of Fe

Table 3. Diffusion coefficients for main sigma stabilizing elements calculated for grain boundaries, as well as lattice diffusion using Eq. (4). Values for lattice diffusion from the DICTRA package are given for reference. For both grain boundary and matrix diffusion, it is assumed that the opposite sides of the particle are growing at the same rate.

Element	D_{GB} cm^{2}s^{-1}	$D_{Lattice}$ cm^{2}s^{-1}	$D_{Lattice}$ (DICTRA) cm^{2}s^{-1}
σ Stabilizers			
Cr	$6.7\cdot10^{-12}$	$2.6\cdot10^{-14}$	$4.7\cdot10^{-14}$
Mo	$2.0\cdot10^{-10}$	$7.8\cdot10^{-13}$	$5.4\cdot10^{-14}$
Matrix Abundant Elements			
Fe	$4.3\cdot10^{-13}$	$1.6\cdot10^{-15}$	$2.0\cdot10^{-14}$
Ni	$4.1\cdot10^{-12}$	$1.6\cdot10^{-14}$	$5.3\cdot10^{-14}$

in the precipitate, see Fig. 8.

5. Conclusions

In this paper, we used a comparatively large set of images in combination with a semi-automated evaluation procedure to acquire precipitation data for a high end austenitic stainless steel aged at 800° C. This made it possible to characterize the precipitates in fraction, number and shape. In particular, it was possible to quantify the particle growth towards the metal matrix as well as at the grain boundary. It was found that the sigma growth was diffusion limited after an initial nucleation period of about 300 s. APT showed very sharp interfaces between the austenite and the sigma phase, consistently narrower than 1 nm. Enrichment of minor elements such as B, C and P were found in the grain boundaries. By combining the growth kinetics from the electron micrographs with atomic resolution composition data on the sigma/austenite interface, it was possible to determine diffusion coefficients for the rate limiting elements that compare well with values found in general databases. The method used in this paper provides a direct measurement of the propagation velocities of the phase boundary, for grain boundary as well as lattice diffusion. The diffusion coefficients along the grain boundary were calculated to about 250 times that of lattice diffusion.

Acknowledgments

Mr. Per Lindström, SMT R&D, is gratefully acknowledged for assistance with heat treatments and sample preparation. Mr. Lars Nylöf and Dr. Raveendra Siriki both contributed with valuable comments on the study. The work in this paper was performed within the FraMat project, a part of the Strategic Materials Program funded by Vinnova - Sweden's innovation agency.

REFERENCES

1) K. Ogawa and T. Osuki: *ISIJ Int.*, **59** (2019), 129. https://doi.org/10.2355/isijinternational.ISIJINT-2018-478
2) K. Ogawa and T. Osuki: *ISIJ Int.*, **59** (2019), 122. https://doi.org/10.2355/isijinternational.ISIJINT-2018-477
3) C.-C. Hsieh and W. Wu: *Int. Scholarly Res. Not.*, **2012** (2012), Article ID. 732471. https://doi.org/10.5402/2012/732471
4) T. Yokoyama, Y. Kataura and T. Ototani: *Tetsu-to-Hagané*, **56** (1970), 772 (in Japanese). https://doi.org/10.2355/tetsutohagane1955.56.6_772
5) T. Nakazawa, S. Hoshino, K. Yamaguchi and Y. Katada: *Tetsu-to-Hagané*, **93** (2007), 240 (in Japanese). https://doi.org/10.2355/tetsutohagane.93.240
6) K. Ogawa and T. Osuki: *ISIJ Int.*, **60** (2020), 1016. https://doi.org/10.2355/isijinternational.ISIJINT-2019-537
7) S. Fukumoto, Y. Oikawa, S. Tsuge and S. Nomoto: *ISIJ Int.*, **50** (2010), 445. https://doi.org/10.2355/isijinternational.50.445
8) A. Zielinski, G. Golanski and M. Sroka: *Mater. Sci. Eng. A*, **796** (2020), 139944. https://doi.org/10.1016/j.msea.2020.139944
9) S. Zhang, H. Li, Z. Jiang, B. Zhang, Z. Li, J. Wu, S. Fan, H. Feng and H. Zhu: *Mater. Charact.*, **152** (2019), 141. https://doi.org/10.1016/j.matchar.2019.04.010
10) J. Erneman, M. Schwind, L. Nylöf, J.-O. Nilsson, H.-O. Andrén and J. Ågren: *Metall. Mater. Trans. A*, **36** (2005), 2595. https://doi.org/10.1007/s11661-005-0257-2
11) A. Perron, C. Toffolon-Masclet, X. Ledoux, F. Buy, T. Guilbert, S. Urvoy, S. Bosonnet, B. Marini, F. Cortial, G. Texier, C. Harder, V. Vignal, P. Petit, J. Farré and E. Suzon: *Acta Mater.*, **79** (2014), 16. https://doi.org/10.1016/j.actamat.2014.06.066
12) A. Jacob, E. Povoden-Karadeniz and E. Kozeschnik: *Calphad*, **60** (2018), 16. https://doi.org/10.1016/j.calphad.2017.10.002
13) A. Jacob and E. Povoden-Karadeniz: Proc. 10th European Stainless Steel Conf. (ESSC 2019), (Vienna), The Austrian Society for Metallurgy and Materials, Leoben, (2019), 250.
14) G. Laplanche, S. Berglund, C. Reinhart, A. Kostka, F. Fox and E. George: *Acta Mater.*, **161** (2018), 338. https://doi.org/10.1016/j.actamat.2018.09.040
15) M. Schwind, J. Källqvist, J.-O. Nilsson, J. Ågren and H.-O. Andrén: *Acta Mater.*, **48** (2000), 2473. https://doi.org/10.1016/S1359-6454(00)00069-0
16) Y.-S. Ji, J. Park, S.-Y. Lee, J.-W. Kim, S.-M. Lee, J. Nam, B. Hwang, J.-Y. Suh and J.-H. Shim: *Mater. Charact.*, **128** (2017), 23. https://doi.org/10.1016/j.matchar.2017.03.030
17) A. D. Warren, R. L. Harniman, Z. Guo, C. M. Younes, P. E. J. Flewitt and T. B. Scott: *J. Mater. Sci.*, **51** (2016), 694. https://doi.org/10.1007/s10853-015-9131-9
18) H.-O. Andrén: *Mater. Sci. Eng. A*, **353** (2003), 62. https://doi.org/10.1016/S0921-5093(02)00668-8
19) R. C. Gonzalez and R. E. Woods: Digital Image Processing, Pearson Education Ltd, Essex, UK, (2018), 811.
20) K. Thompson, D. Lawrence, D. Larson, J. Olson, T. Kelly and B. Gorman: *Ultramicroscopy*, **107** (2007), 131. https://doi.org/10.1016/j.ultramic.2006.06.008
21) F. G. Cottrell: *Z. Phys. Chem.*, **42U** (1903), 385. https://doi.org/10.1515/zpch-1903-4229
22) J.-O. Andersson, T. Helander, L. Höglund, P. Shi and B. Sundman: *Calphad*, **26** (2002), 273. https://doi.org/10.1016/S0364-5916(02)00037-8
23) B. Jönsson: *Z. Metallkd.*, **86** (1995), 686.
24) A. Paul, K. Kaimal, M. Naik and S. Dharwadkar: *J. Nucl. Mater.*, **217** (1994), 75. https://doi.org/10.1016/0022-3115(94)90306-9
25) J. Cermak: *Z. Metallkd.*, **81** (1990), 193.
26) M. Mizouchi, Y. Yamazaki, Y. Iijima and K. Arioka: *Mater. Trans.*, **45** (2004), 2945. https://doi.org/10.2320/matertrans.45.2945
27) Z. Tökei, K. Hennesen, H. Viefhaus and H. Grabke: *Mater. Sci. Technol.*, **16** (2000), 1129. https://doi.org/10.1179/026708300101507055
28) A. F. Smith: *Met. Sci.*, **9** (1975), 375. https://doi.org/10.1179/030634575790444270
29) C. Herzig and S. V. Divinski: *Mater. Trans.*, **44** (2003), 14. https://doi.org/10.2320/matertrans.44.14
30) T. Prasanthi, C. Sudha, S. Raju and S. Saroja: *J. Alloys Compd.*, **808** (2019), 151726. https://doi.org/10.1016/j.jallcom.2019.151726